International Journal of Fracture **81:** 321–341, 1996.
© 1996 *Kluwer Academic Publishers. Printed in the Netherlands.*

A finite element analysis of plane strain dynamic crack growth at a ductile-brittle interface

KALLOL DAS* and R. NARASIMHAN**
Department of Mechanical Engineering, Indian Institute of Science, Bangalore 560012, India

Received 12 March 1996; accepted in revised form 20 September 1996

Abstract. In this work, steady, dynamic crack growth under plane strain, small-scale yielding conditions along a ductile-brittle interface is analysed using a finite element procedure. The ductile solid is taken to obey the J_2 flow theory of plasticity with linear isotropic strain hardening, while the substrate is assumed to exhibit linear elastic behaviour. The objectives of this work are to establish the validity of an asymptotic solution for this problem which has been derived recently [12], and to examine the effect of changing the remote (elastic) mode-mixity on the near-tip fields. Also, the influence of crack speed on the stress fields and crack opening profiles near the propagating interface crack tip is assessed for various bi-material combinations. Finally, theoretical predictions are made for the variation of the dynamic fracture toughness with crack speed for crack growth under a predominantly tensile mode along ductile-brittle interfaces. Attention is focused on the effect of mismatch in stiffness and density of the constituent phases on the above aspects.

1. Introduction

In recent years, there has been an increase in the technological application of multiphase components like electronic packaging, thin films and protective coatings. These components fail, most commonly, by debonding of the constituent phases along the interfaces. In recent experimental studies (see, for example [1]), crack speeds far higher than those attainable in homogeneous solids have been observed during crack propagation along interfaces. Hence, it is important to understand the mechanics of dynamic crack propagation along a ductile-brittle interface.

Castañeda and Mataga [2] and Drugan [3] derived the asymptotic fields for quasi-static crack growth at a ductile-brittle interface. Castañeda and Mataga [2] assumed the ductile phase to exhibit linear strain hardening or perfect plasticity, and the brittle phase to be linear elastic or rigid. For all the above cases, they obtained two asymptotic solutions for interfacial crack growth with distinct values of near-tip mode-mixity, $m = 2/\pi \tan^{-1}(\sigma_{22}/\sigma_{12})$, where σ_{22}/σ_{12} is the ratio of the normal to shear traction on the interface line just ahead of the tip. One solution resembled the Mode I field in homogeneous elastic-plastic solids with m close to unity, and was called a *tensile solution*. The other solution resembled the Mode II field in homogeneous elastic-plastic solids with m close to zero and was called a *shear solution*. Drugan [3], while considering the perfectly plastic model for the ductile phase and a rigid substrate, found a family of asymptotic fields that exhibits a range of values for the near-tip mode-mixity m. This was made possible by permitting physically acceptable discontinuities in the near-tip velocity fields.

Several investigators [4–6] have obtained analytical asymptotic solutions for dynamic crack growth in homogeneous elastic-plastic solids. Also, many finite element studies (see, for example, [7, 8]) have been conducted to validate these asymptotic solutions and to investigate

* Graduate student.
** Associate professor.

the effect of inertia in enhancing the resistance of an elastic-plastic material to high speed crack growth. Dynamic crack growth along an interface between two dissimilar elastic solids with arbitrary anisotropy was sudied by Yang et al. [9]. Deng [10] has proposed some families of asymptotic fields for plane strain dynamic crack growth at the interface between an elastic-ideally plastic solid and a rigid substrate, as well as between two dissimilar elastic-ideally plastic solids.

In some very recent studies, Ranjith and Narasimhan [11, 12] derived the asymptotic fields for dynamic crack growth at the interface between a linear hardening ductile phase and a brittle substrate under anti-plane strain and plane strain conditions. They assumed variable-separable solutions for the stress and velocity components in the form,

$$\sigma_{ij} = A\sigma_0^{(1)}\tilde{\sigma}_{ij}(\theta)r^s, \tag{1}$$

$$v_i = AV\epsilon_0^{(1)}\tilde{v}_i(\theta)r^s/s, \tag{2}$$

where r, θ are polar coordinates centered at the crack tip. In the above equation, A denotes an amplitude factor (which is undetermined from the asymptotic analysis), s a singularity exponent, V the crack speed, $\sigma_0^{(1)}$ and $\epsilon_0^{(1)}$ the initial yield stress and strain of the ductile phase. They found two solutions (a tensile-type and a shear-type) for each crack speed and strain hardening level of the ductile phase in the analysis of the plane strain problem [12]. As in the quasi-static case [2], the above two solutions are characterized by distinct near-tip mixities m close to unity and zero.

However, Ranjith and Narasimhan [12] were able to obtain variable-separable solutions only between a lower and upper bound of the strain hardening level of the ductile phase for each crack speed. As the strain hardening level approaches the upper bound (at a given crack speed), the tensile and shear solutions were found to approach each other and to *coalesce* to the same field. However, when the two phases have identical elastic properties, no such phenomenon of coalescence was observed. The analytical, asymptotic solution of Ranjith and Narasimhan [12] has several drawbacks. First, a variable-separable form is assumed with a power law singularity in the radial coordinate as given in eqs. (1) and (2). Secondly, even if the above singular solution is valid, its range of dominance near the crack tip is unknown. Finally, considering small-scale yielding conditions, the range of remote (elastic) mode-mixities which results in a near-tip tensile or shear field has to be investigated. The last two issues noted above are expected to depend on the bi-material properties such as stiffness or density ratio of the two phases and strain hardening of the ductile phase, as well as crack speed.

Thus, the objective of the present work is to perform full-field finite element simulations of steady dynamic crack growth under plane strain, small-scale yielding conditions along the interface between a linear hardening elastic-plastic solid and a brittle solid. The simulations will be carried out for different remote (elastic) mode-mixities, different bi-material combinations and various crack speeds. The finite element results will be used to address the issues noted above in connection with the asymptotic analysis of Ranjith and Narasimhan [12]. Also, the effect of crack speed on the near-tip stress fields, crack profiles and plastic zones will be examined for different bi-material combinations. Finally, theoretical predictions for the variation of dynamic fracture toughness with crack speed for interface crack growth under a predominantly tensile mode will be made from the finite element results. The effect of the strain hardening level of the ductile phase and mismatch in elastic stiffness of the two solids on the above relationship will be studied.

2. Numerical procedure

2.1. Finite element formulation

The finite element formulation employed in the present investigation to simulate steady dynamic crack growth under plane strain, small-scale yielding conditions is based on moving crack tip coordinates and is similar to the one used in [7]. Only a brief review is given in this paper.

A semi-infinite crack which has grown along the interface between a ductile phase (referred to below as material #1) and a brittle material (designated here as material #2) at a speed V for a long enough time is considered, so that all transients associated with crack initiation have died out. A steady mechanical state is then established with respect to the moving crack tip. Further, small-scale yielding conditions are assumed such that the zone of plastic deformation in the ductile phase is contained in a small region near the crack tip and the elastodynamic **K**-field [9] holds good at points far away from the crack tip. The following normalizations are used for the crack tip coordinates (x_1, x_2), displacements u_i, stresses σ_{ij}, strains ϵ_{ij} and velocities v_i:

$$\left.\begin{aligned}
\widehat{x}_i &= x_i/(|\mathbf{K}|/\sigma_0^{(1)})^2 \\
\widehat{u}_i &= u_i/(|\mathbf{K}|^2/E^{(1)}\sigma_0^{(1)}) \\
\widehat{\varepsilon}_{ij} &= \epsilon_{ij}/\epsilon_0^{(1)} \\
\widehat{\sigma}_{ij} &= \sigma_{ij}/\sigma_0^{(1)} \\
\widehat{v}_i &= v_i/(V\epsilon_0^{(1)})
\end{aligned}\right\}. \tag{3}$$

In the above equation, $\sigma_0^{(1)}$ is the initial yield stress of the ductile material, $\epsilon_0^{(1)} = \sigma_0^{(1)}/E^{(1)}$ is its initial yield strain and $E^{(1)}$ its Young's modulus. Also, $|\mathbf{K}|$ is the magnitude of the remote dynamic stress intensity factor which is a complex quantity for interface crack growth [9]. Here, the plane $x_2 = 0$ corresponds to the interface and the crack grows in the positive x_1 direction. Finally, $\beta = V/C^{(1)}$ denotes a normalized crack speed, where $C^{(1)} = \sqrt{E^{(1)}/\rho^{(1)}}$ is the elastic bar wave speed and $\rho^{(1)}$ the density of the ductile phase. In this work, the steady-state condition $(\dot{\ }) = \partial(\,)/\partial t = -V\partial(\,)/\partial x_1$ is invoked to simplify the governing equations.

On utilizing the above normalization in the equations of motion, and applying the virtual work principle, the following finite element equation may be obtained [7]

$$\underline{KU} = \underline{F} + \underline{R}, \tag{4}$$

where $\underline{U}$ is the vector of nodal point displacements. The stiffness matrix $\underline{K}$ and the force vectors $\underline{F}$ and $\underline{R}$ in the above equations are defined as

$$\underline{K} = \int_V \underline{B}^T \underline{\widehat{C}B}\,\mathrm{d}V - \beta^2 \int_V \widehat{\rho}\frac{\partial \underline{N}^T}{\partial \widehat{x}_1}\frac{\partial \underline{N}}{\partial \widehat{x}_1}\,\mathrm{d}V, \tag{5}$$

$$\underline{F} = \int_{S_T} \underline{N}^T \left[\underline{\widehat{T}} - \widehat{\rho}\beta^2 \frac{\partial \underline{\widehat{u}}}{\partial \widehat{x}_1} n_1\right] \mathrm{d}S, \tag{6}$$

$$\underline{R} = \int_V \underline{B}^T \underline{\widehat{C}} \underline{\epsilon}^{\widehat{p}} \, \mathrm{d}V. \tag{7}$$

In the above equation, $\widehat{\underline{T}}$ is the normalized traction vector acting on the portion S_T of the boundary (of domain V) whose outward normal is $\underline{n}$. Further, $\widehat{\underline{C}}$ denotes the elasticity tensor normalized by the Young's modulus $E^{(1)}$ of the ductile phase and $\widehat{\rho}$ is the density normalized by $\rho^{(1)}$. Thus, $\widehat{\rho} = 1$ when a material point lies in the ductile phase and $\widehat{\rho} = \rho^{(2)}/\rho^{(1)}$ if it lies in the elastic substrate. For the ductile phase, an additive decomposition of the total strains into elastic and plastic parts ($\widehat{\underline{\epsilon}} = \widehat{\underline{\epsilon}}^e + \widehat{\underline{\epsilon}}^p$) is assumed here. Also, $\underline{N}$ and $\underline{B}$ are the shape function matrix and strain-displacement matrix, respectively. It is noted that the solutions are carried out under 2-D plane strain conditions.

In this paper, the brittle material (material #2) is assumed to obey linear isotropic elasticity. The ductile phase (material #1) on the other side of the interface is taken to obey the J_2 flow theory of plasticity with linear isotropic strain hardening. The initial yield stress of this phase is denoted as $\sigma_0^{(1)}$ and its tangent modulus as $E_t^{(1)}$. In presenting the results in the next section, a hardening parameter $\alpha = E_t^{(1)}/E^{(1)}$ will be used.

2.2. Computational Aspects

The dominant term in the stress and displacement fields near a dynamically propagating crack tip at the interface between two dissimilar linear elastic materials is scaled be a complex stress intensity factor **K** [9]. These fields are expressed in polar coordinates (r, θ) with the origin at the crack tip in the following form [9, 13]:

$$\sigma_{ij}(r,\theta) = \frac{\mathcal{R}e\{\mathbf{K}r^{i\varepsilon}\}}{\sqrt{2\pi r}}\tilde{\sigma}_{ij}^1(\theta;\varepsilon;V) + \frac{\mathcal{I}m\{\mathbf{K}r^{i\varepsilon}\}}{\sqrt{2\pi r}}\tilde{\sigma}_{ij}^2(\theta;\varepsilon;V), \tag{8}$$

$$u_i(r,\theta) = \frac{\mathcal{R}e\{\mathbf{K}r^{i\varepsilon}\}}{\mu}\sqrt{\frac{2r}{\pi}}\tilde{u}_i^1(\theta;\varepsilon;V) + \frac{\mathcal{I}m\{\mathbf{K}r^{i\varepsilon}\}}{\mu}\sqrt{\frac{2r}{\pi}}\tilde{u}_i^2(\theta;\varepsilon;V). \tag{9}$$

Here, $\tilde{\sigma}_{ij}^{(\alpha)}$ and $\tilde{u}_i^{(\alpha)}$ denote dimensionless angular functions of stress and displacements and μ is the shear modulus of the appropriate material. The bi-material constant ε is a function of the elastic properties of the two materials and the crack speed V. The above angular functions and ε are given in [9, 13].

It is clear from (8) that the tension and shear effects are inseparable near an interface crack tip. A measure of the relative proportion of shear to normal tractions on the interface requires the specification of a length quantity. Thus the mode-mixity ψ is specified by

$$\tan\psi = \frac{\sigma_{12}(L,0)}{\sigma_{22}(L,0)} = \frac{\mathcal{I}m\{\mathbf{K}L^{i\varepsilon}\}}{\mathcal{R}e\{\mathbf{K}L^{i\varepsilon}\}} = \tan(\psi_0 + \varepsilon\ln L), \tag{10}$$

where $\psi_0 = \tan^{-1}(\mathcal{I}m\{\mathbf{K}\}/\mathcal{R}e\{\mathbf{K}\})$ is the phase of **K**. The length L is arbitrary. The difference in ψ due to changing L from L_1 to L_2 is given by

$$\psi_2 - \psi_1 = \varepsilon\ln(L_2/L_1). \tag{11}$$

In the present small-scale yielding formulation, (8), (9) after normalizing according to (3), are applied as boundary conditions on the outermost boundary of a large circular domain with

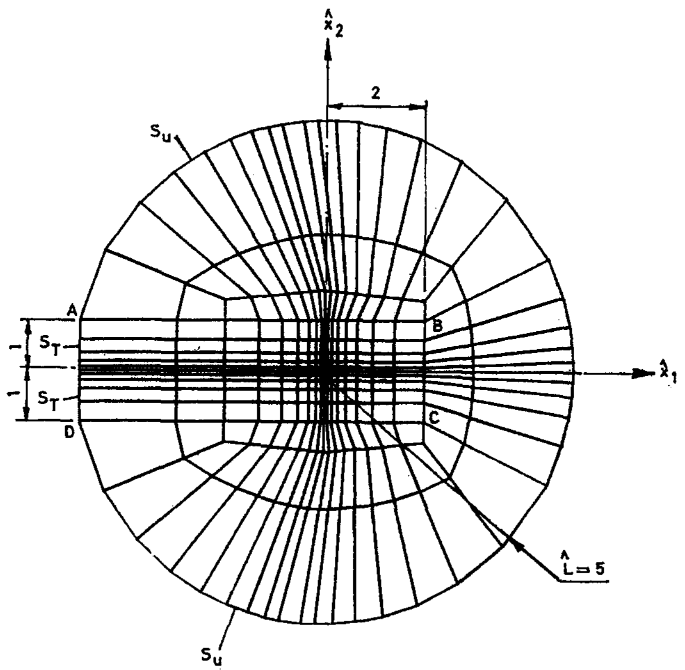

Figure 1. A coarse representation of the finite element mesh.

radius L. The domain modelled along with a coarse representation of the finite element mesh is shown in Figure 1. In this figure, the interface is located along $\widehat{x}_2 = 0$ and the crack line along $(\widehat{x}_2 = 0, \widehat{x}_1 < 0)$. The upper half (i.e., $\widehat{x}_2 > 0$) denotes the ductile phase (material #1), and the lower half (i.e., $\widehat{x}_2 < 0$) the brittle phase. Since $(|\mathbf{K}|/\sigma_0^{(1)})^2$ is the only relevant length parameter in the small-scale yielding formulation, all mesh dimensions are normalized by it (see also (3)).

Displacement boundary conditions based on the elastic field (9) are specified on the portion S_u of the outer boundary which is a circular arc of normalized radius $\widehat{L} = 5$ centered at the crack tip. It will be found in Section 3 that the maximum plastic zone size obtained in any computation performed here is within $0.8(|\mathbf{K}|/\sigma_0^{(1)})^2$. Thus, $\widehat{L}$ is more than six times the (normalized) size of the active plastic zone, which ensures that small-scale yielding conditions prevail. The computations reported here are carried out for different values of ψ and normalized crack speed β corresponding to various bi-material combinations. For all the bi-material combinations the Poisson's ratio is assumed as $\nu^{(1)} = \nu^{(2)} = 0.3$. It must be noted that the value of ψ given according to (10) depends on the above chosen value of L (i.e., $5(|\mathbf{K}|/\sigma_0^{(1)})^2$), except for the bi-material with $E^{(1)}/E^{(2)} = 1, \rho^{(1)}/\rho^{(2)} = 1$ which has $\varepsilon \equiv 0$. If an alternate length scale is desired to be used in defining ψ, then its value must be appropriately modified according to eq. (11). Traction boundary conditions based on (9) are prescribed on the portion S_T of the boundary in Figure 1.

An important aspect in the numerical formulation of elastic-plastic problems is the algorithm used for updating internal variables, plastic strains and stresses. In the present steady-state formulation, these quantities at a certain material point $(\widehat{x}_1, \widehat{x}_2)$ are obtained by integrating the rate constitutive equations from the elastic-plastic boundary in the negative $\widehat{x}_1$ direction, along a line holding $\widehat{x}_2$ constant. The stress update algorithm used here is the *Tangential*

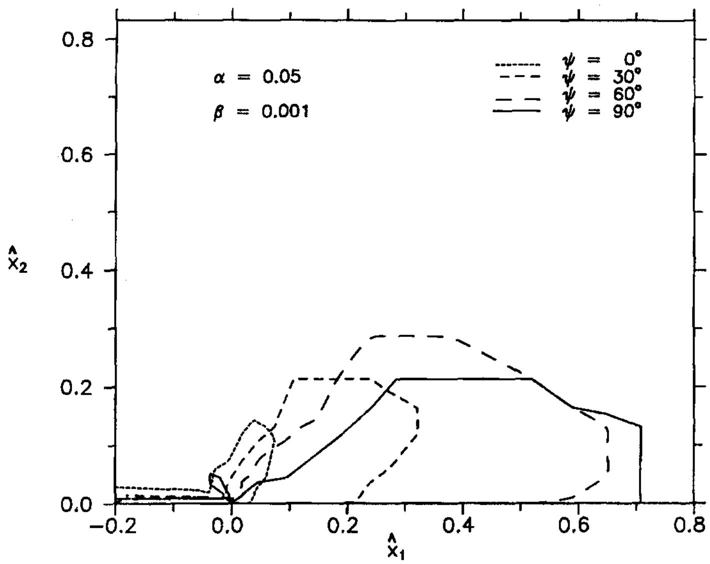

Figure 2. Active plastic zones surrounding the crack tip propagating with normalized velocity $\beta = 0.001$ for the bi-material with $E^{(1)}/E^{(2)} = 1, \rho^{(1)}/\rho^{(2)} = 1, \alpha = 0.05$.

Predictor – Radial Return method with subincrementation [14]. In order to facilitate the above integration, a rectangular portion ABCD consisting of rectangular elements aligned parallel to the interface line is used as shown in Figure 1 such that all plastic deformation including the wake region is always contained within it. It is noted that it is inappropriate to specify the elastodynamic **K**-field as boundary condition on the portion of the downstream (left) boundary which coincides with the wake region (portion S_T in Figure 1). However, it is felt that its effect may be only negligible as far as the near-tip fields are concerned. This is because, as will be seen in Section 3, the vertical height of the wake region is quite small (of the order of 0.2 to 0.3 $(|\mathbf{K}|/\sigma_0^{(1)})^2$).

As shown in the coarse mesh of Figure 1, four-noded isoparametric quadrilateral elements are employed. A mesh consisting of 2238 elements and 2348 nodes was used in the computations. The mesh is graded near the tip with the smallest element size equal to $2 \times 10^{-6}(|\mathbf{K}|/\sigma_0^{(1)})^2$, which is very much smaller than the plastic zone size. Thus, the near-tip fields are expected to be resolved quite accurately by this mesh, as will be confirmed in Section 3 when comparisons are made with the analytical solution [12].

The force vector $\underline{R}$ in (4) involves the plastic strain $\bar{\epsilon}^p$ (see(7)) which is unknown *apriori*. Hence, an iterative procedure described in [15] is used to solve (4). The *B-Bar* method proposed by Hughes [16] is employed to treat nearly incompressible deformation under plane strain condition, which would otherwise result in an over-stiff response in the finite element grid.

3. Results and discussion

3.1. Plastic zones

The active plastic zones corresponding to different far-field mixities ψ for the bi-material with $E^{(1)}/E^{(2)} = 1, \rho^{(1)}/\rho^{(2)} = 1, \alpha = 0.05$ at crack speed $\beta = 0.001$ in normalized

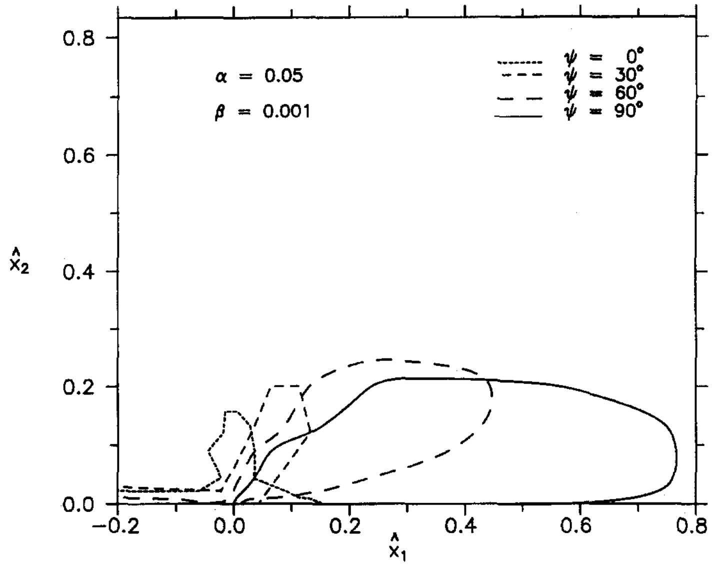

Figure 3. Active plastic zones surrounding the crack tip propagating with normalized velocity $\beta = 0.001$ for the bi-material with $E^{(1)}/E^{(2)} = 0.2, \rho^{(1)}/\rho^{(2)} = 1, \alpha = 0.05$.

crack tip coordinates $\hat{x}_1, \hat{x}_2$ are shown in Figure 2. It can be seen from this figure that the plastic zone ahead of the crack tip increases from about $0.035(|\mathbf{K}|/\sigma_0^{(1)})^2$ to $0.7(|\mathbf{K}|/\sigma_0^{(1)})^2$ as ψ increases from 0° to 90°. The height of the plastic zone above the interface increases from $0.15(|\mathbf{K}|/\sigma_0^{(1)})^2$ to $0.3(|\mathbf{K}|/\sigma_0^{(1)})^2$ as ψ increases from 0° to 60°, but decreases to $0.2(|\mathbf{K}|/\sigma_0^{(1)})^2$ at $\psi = 90°$. Further, for ψ in the range from 0° to 60°, a secondary plastic reloading zone adjacent to the crack line is present. The height of this secondary plastic zone decreases with an increase in ψ from 0° to 60°. Interestingly, a tiny tail-like trailing portion is present at an angle of about 130° with respect to the crack tip for $\psi = 90°$.

The results at high crack speed for this bi-material showed that the size of the plastic zone ahead of the crack tip is not affected to any appreciable extent. But the effect of crack speed is manifested by an increase in the height of the plastic zone by about 30%, as well as the height of the secondary plastic region for the cases $\psi = 0°$ and 30°. Further, the length of the trailing tail-like portion for $\psi = 90°$ increases significantly in length as β increases.

The plastic zones for the bi-material with $E^{(1)}/E^{(2)} = 0.2$ and $\rho^{(1)}/\rho^{(2)} = 1$ at a crack speed of $\beta = 0.001$ are shown in Figure 3. In interpreting the plastic zones in this figure, it must be noted that the values of ψ are based on a length scale $L = 5(|\mathbf{K}|/\sigma_0^{(1)})^2$ (see Figure 1). On comparing it with Figure 2, it can be seen that the size of the plastic zone corresponding to the case $\psi = 0°$ for the bi-material with $E^{(1)}/E^{(2)} = 0.2$ is significantly larger in front of the crack tip. This feature may also be observed in the stationary interface crack results of Shih and Asaro [17] for the case of a rigid substrate. The overall size of the plastic zones for $\psi = 30°$ and 60° is smaller in Figure 3 as compared to Figure 2. But the plastic zone boundary corresponding to $\psi = 90°$ is larger ahead of the tip for $E^{(1)}/E^{(2)} = 0.2$. However, the trailing tail-like portion for $\psi = 90°$ is absent corresponding to the bi-material with $E^{(1)}/E^{(2)} = 0.2$.

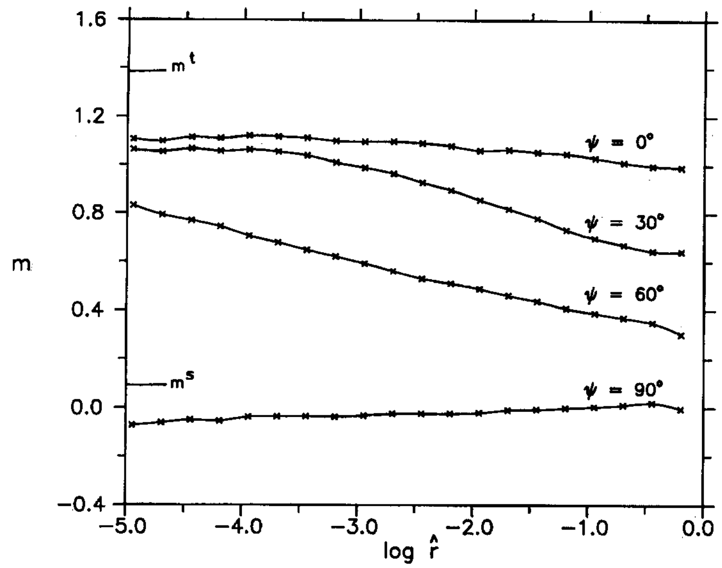

Figure 4. Variation of the mode-mixity parameter m with radial distance ahead of the crack tip for various values of remote ψ at $\beta = 0.25$. The material parameters are $E^{(1)}/E^{(2)} = 1, \rho^{(1)}/\rho^{(2)} = 1, \alpha = 0.25$. The corresponding asymptotic mode-mixities obtained from the analytical tensile and shear solutions are also indicated by m^t and m^s, respectively.

3.2. EFFECT OF FAR-FIELD MIXITY ON NEAR-TIP MIXITY

The effect of far-field (elastic) mode-mixity ψ on the near-tip mixity will be examined in this section. To this end, the variations of the mode-mixity parameter $m(\hat{r}) = (2/\pi)\tan^{-1}(\sigma_{\theta\theta}(\hat{r}, 0)/\sigma_{r\theta}(\hat{r}, 0))$ with $\log \hat{r}$ for different far-field mixities ψ at crack speed $\beta = 0.25$ for the bi-material with $E^{(1)}/E^{(2)} = 1, \rho^{(1)}/\rho^{(2)} = 1, \alpha = 0.25$ are shown in Figure 4. At a sufficiently large distance from the crack tip, where the elastodynamic **K**-field prevails, $m(\hat{r})$ in this figure approaches the value determined by the prescribed ψ (in degrees), which is given by $m = 1 - \psi/90°$. It can be seen from Figure 4 that as the crack tip is approached, m tends to a definite limit of around 1.1 for $\psi = 0°$ and 30°. This limiting value is close to that corresponding to the asymptotic tensile solution of [12] which is indicated as m^t in the figure. On the other hand, m approaches a limit of around −0.1 near the crack tip for $\psi = 90°$. This value is close to that obtained from the asymptotic shear solution [12] which is marked as m^s in the figure. For the case $\psi = 60°, m(\hat{r})$ increases monotonically as $\hat{r} \to 0$ and appears to be approaching the limit set by the asymptotic tensile solution. It is clear that for this bi-material, a transition in the character of the near-tip solution from a tensile to a shear-type field occurs between $\psi = 60°$ and 90°.

The variations of $m(\hat{r})$ with $\log \hat{r}$ for the bi-material with $E^{(1)}/E^{(2)} = 0.2, \rho^{(1)}/\rho^{(2)} = 1, \alpha = 0.25$ at crack speed $\beta = 0.001$ corresponding to different remote mixities ψ are displayed in Figure 5. Since the asymptotic solution of [12] at high crack speed is not available for this bi-material, results are presented for the quasi-static case. The nature of the curves in this figure are quite different from those shown in Figure 4 for the case $E^{(1)}/E^{(2)} = 1$. First, an asymptotic limit for m (of around 1.2) is attained at a much larger distance from the tip (in the range of $\hat{r} = 10^{-3}$ to 10^{-1}) for ψ ranging from 0° to 60° in Figure 5. This asymptotic limit is close to that predicted by the tensile analytical solution [12], which is

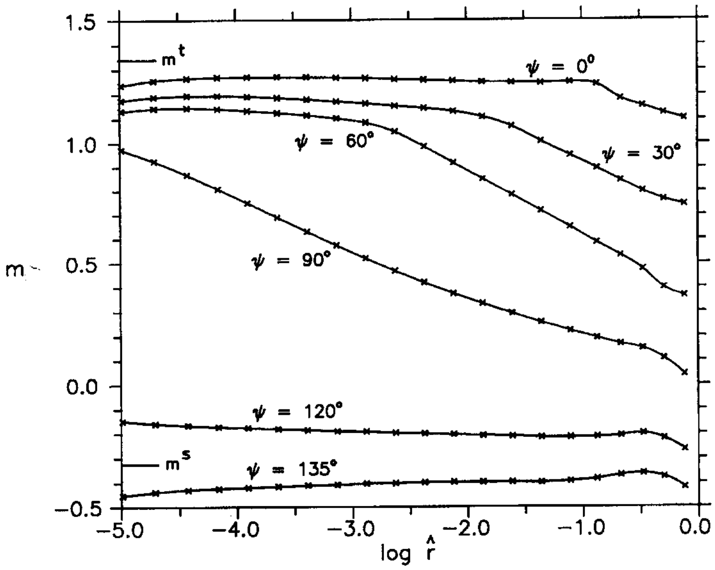

Figure 5. Variation of the mode-mixity parameter m with radial distance ahead of the crack tip for various values of remote ψ at $\beta = 0.001$. The material parameters are $E^{(1)}/E^{(2)} = 0.2, \rho^{(1)}/\rho^{(2)} = 1, \alpha = 0.25$. The corresponding asymptotic mode-mixities obtained from the analytical tensile and shear solutions are also indicated by m^t and m^s, respectively.

shown by m^t in the figure. Secondly, unlike in Figure 4, $m(\hat{r})$ for the case $\psi = 90°$, increases monotonically as $\hat{r} \to 0$ and appears to be approaching the same asymptotic limit attained by the curves corresponding to $\psi = 0°$ to $60°$. On the other hand, it is found that the curves pertaining to $\psi = 120°$ and $135°$ (which correspond to cases where the remote normal stress on the interface line is compressive) approach near-tip value of m which are negative. In particular, the near-tip value of m obtained for $\psi = 135°$ in Figure 5 is close to that predicted by the analytical shear solution which is marked as m^s. Bose and Castañeda [18] who also investigated this issue, did not examine the cases with remote $\psi > 90°$, and concluded that a shear near-tip field is not attained for quasi-static crack growth at a bi-material interface with a rigid substrate. The finite element results displayed in Figures 4 and 5 were not affected significantly by crack speed.

3.3. Validation of Asymptotic Solutions

It must be recalled that the asymptotic solutions of [12] involve two key assumptions. First, the dominant term of the stress and velocity components are assumed to be variable-separable in polar coordinates r, θ centered at the crack tip. Secondly, a power singularity (of the type r^s) in the radial variation of the dominant term is assumed. In this section, the validity of the above assumptions is examined, and the range of dominance of the asymptotic solutions is investigated by comparing them with the results of the full-field finite element analyses.

First, the radial dependence of the near-tip stress field is examined. The variation of $\ln(\hat{\sigma}_{\theta\theta})$ with $\ln(\hat{r})$ along $\theta = 0°$ and $45°$ with respect to the crack tip, obtained from the finite element solutions corresponding to $\psi = 0°$ at $\beta = 0.001$, are shown in Figure 6 for the bi-material combination with $E^{(1)}/E^{(2)} = 1,\ \rho^{(1)}/\rho^{(2)} = 1,\ \alpha = 0.25$. It should be recalled that the near-tip mixity is close to that predicted by the tensile solution for $\psi = 0°$. The radial variation

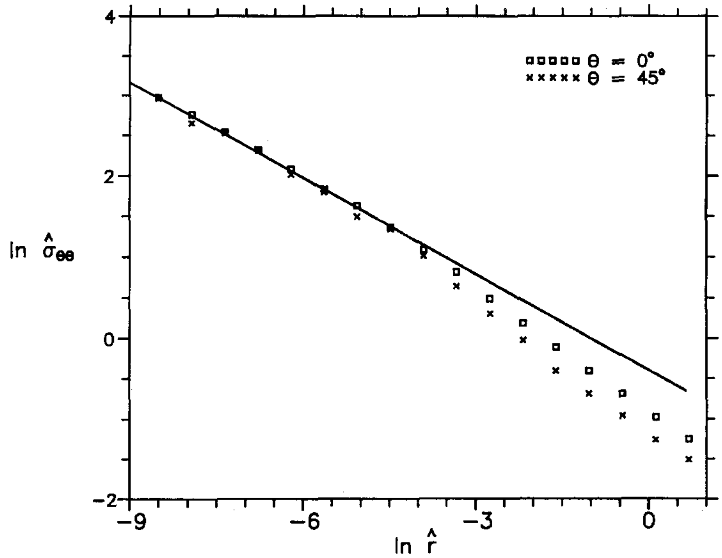

Figure 6. Logarithmic plot of the radial variation of $\widehat{\sigma}_{\theta\theta}$ at two different angles for the bi-material with $E^{(1)}/E^{(2)} = 1, \rho^{(1)}/\rho^{(2)} = 1, \alpha = 0.25$ at $\psi = 0°, \beta = 0.001$. The solid straight lines correspond to best fits having slopes equal to the singularity strengths of the corresponding analytical tensile solutions.

along the 45° line is extracted after performing a post-process smoothening procedure [19]. It must be noted first that the variation of $\widehat{\sigma}_{\theta\theta}$ along $\theta = 0°$ and 45° in this plot are virtually indistinguishable. Further, the finite element results show that the tangential stress $\widehat{\sigma}_{\theta\theta}$ varies linearly in log-log coordinates with distance near the crack tip. Hence, straight line fits were made to the finite element results for the variation of $\ln(\widehat{\sigma}_{\theta\theta})$ with $\ln(\widehat{r})$, from which the near-tip singularity exponents, as predicted by the finite element procedure along $\theta = 0°$ and 45°, were obtained as the slope. These will be denoted below as s^1 and s^2, respectively.

Next, straight line fits with slope equal to the singularity order s^* corresponding to the asymptotic tensile solution of [12] were made to the same finite element data points. The amplitude factor A in eq. (1) was determined from this straight line fit along $\theta = 0°$ since $\widetilde{\sigma}_{\theta\theta}(\theta = 0°)$ is assumed as unity in the asymptotic tensile solution derived in [12]. The normalized distance $\widehat{r}_D^1$ and $\widehat{r}_D^2$ along $\theta = 0°$ and 45°, respectively, from the crack tip, where the difference between the points obtained from the numerical solution and the above fitted straight lines exceeds an allowable deviation (say, 5%) is taken as a measure of the range of dominance of the tensile solution. In a similar manner, the singularity strength and range of dominance of the shear solution are determined, using the radial variation of $\widehat{\sigma}_{r\theta}$ corresponding to the remote ψ which gives rise to a near-tip mixity close to that predicted by the analytical shear solution. Here, $\widehat{\sigma}_{r\theta}$ is used instead of $\widehat{\sigma}_{\theta\theta}$, since $\widehat{\sigma}_{r\theta}$ plays the dominant role in the shear-type solution.

The values of s^1, s^2, $\widehat{r}_D^1$ and $\widehat{r}_D^2$, thus extracted from the finite element results for the case $\psi = 0°$ corresponding to the bi-material with $E^{(1)}/E^{(2)} = 1, \rho^{(1)}/\rho^{(2)} = 1$, are summarized along with the singularities s^* of the analytical tensile solution [12] in Table 1. Results are presented in this table corresponding to different α values and different crack speeds β. It can be seen from this table that the finite element results for the singularity exponents match quite well the analytical values s^* irrespective of α and β. Further, the strength of the singularity $|s|$ for the tensile field decreases as the strain hardening parameter α decreases at a given crack

Table 1. Singularity exponent s obtained from finite element analysis with $\psi = 0°$ and the corresponding analytical tensile results, as well as the range of dominance $\hat{r}_D$ of the tensile solution obtained from the radial variation of $\sigma_{\theta\theta}$ component of stress. Superscripts 1 and 2 of s and $\hat{r}_D$ denote the corresponding values estimated along $\theta = 0°$ and 45°, respectively. The analytically obtained s is shown by s^*. Non-availability of analytical solution is pointed out by N.A. The material parameters are $E^{(1)}/E^{(2)} = 1, \rho^{(1)}/\rho^{(2)} = 1$.

		β							
α		0.001		0.15		0.20		0.25	
		s	$\hat{r}_D$	s	$\hat{r}_D$	s	$\hat{r}_D$	s	$\hat{r}_D$
	s^*	−0.4415		−0.4351		−0.4289		−0.4181	
0.40	s^1 & $\hat{r}_D^1$	−0.4351	0.0206	−0.4294	0.0175	−0.4165	0.0173	−0.4076	0.0131
	s^2 & $\hat{r}_D^2$	−0.4569	0.0038	−0.4517	0.0037	−0.4468	0.0038	−0.4352	0.0027
	s^*	−0.4151		−0.4048		−0.3940		−0.3747	
0.30	s^1 & $\hat{r}_D^1$	−0.4041	0.0194	−0.3930	0.0167	−0.3834	0.0144	−0.3664	0.0111
	s^2 & $\hat{r}_D^2$	−0.4218	0.0045	−0.4100	0.0043	−0.4019	0.0043	−0.3830	0.0038
	s^*	−0.3693		−0.3499		−0.3270			
0.20	s^1 & $\hat{r}_D^1$	−0.3558	0.0174	−0.3341	0.0147	−0.3134	0.0116	N.A.	
	s^2 & $\hat{r}_D^2$	−0.3680	0.0061	−0.3450	0.0055	−0.3238	0.0052		
	s^*	−0.2696		−0.2064					
0.10	s^1 & $\hat{r}_D^1$	−0.2695	0.0109	−0.2049	0.0020	N.A.		N.A.	
	s^2 & $\hat{r}_D^2$	−0.2702	0.0063	−0.1899	0.0016				
	s^*	−0.1889							
0.05	s^1 & $\hat{r}_D^1$	−0.1814	0.0068	N.A.		N.A.		N.A.	
	s^2 & $\hat{r}_D^2$	−0.1888	0.0003						

speed β, and also as β increases at a fixed α. The latter effect is more pronounced at low values of α.

Table 2 contains similar results obtained from the finite element solution corresponding to $\psi = 90°$ for the same bi-material along with s^* predicted by the analytical shear solution. As in Table 1, the agreement between the values s^1 and s^2 determined from the finite element solution at $\theta = 0°$ and 45° with the analytical results s^* is good, except perhaps at low values of α. It can be observed from Table 2 that $|s|$ decreases with a decrease in α at a fixed β. But the effect of increase in crack speed β at a fixed α on s is negligible in contrast to the tensile solution of Table 1. On comparing Tables 1 and 2, it can be noticed that at a given crack speed, $|s|$ for the tensile solution is higher than that of shear solution for high values of α, whereas the reverse holds at a low α. Further, the above cross-over of $|s|$ of the tensile and shear fields happens at a higher α as crack speed increases.

Table 3 summarizes the s and $\hat{r}_D$ values extracted from the finite element results for $\psi = 0°$ corresponding to the bi-material combination with $E^{(1)}/E^{(2)} = 0.2$ and $\rho^{(1)}/\rho^{(2)} = 1$. The singularity exponent s^* determined from the corresponding analytical tensile solution is also presented. Only limited data is given in this table, since it is possible to obtain the analytical tensile solution only for a very limited range of α between a lower and an upper bound for a given crack speed β (see [12]). It can be seen from this table that the trend of variation of s with α and β is similar to the case with $E^{(1)}/E^{(2)} = 1$ presented in Table 1. Further, a comparison of Tables 1 and 3 reveals that the strength of singularity is less when the substrate is stiffer irrespective of α and β.

Table 2. Singularity exponent s obtained from finite element analysis with $\psi = 90°$ and the corresponding analytical shear results, as well as the range of dominance $\hat{r}_D$ of the shear solution obtained from the radial variation of $\sigma_{r\theta}$ component of stress. Notations are some as in Table 1. The material parameter are $E^{(1)}/E^{(2)} = 1, \rho^{(1)}/\rho^{(2)} = 1$.

α		β							
		0.001		0.15		0.20		0.25	
		s	$\hat{r}_D$	s	$\hat{r}_D$	s	$\hat{r}_D$	s	$\hat{r}_D$
	s^*	−0.4298		−0.4297		−0.4296		−0.4295	
0.40	s^1 & $\hat{r}_D^1$	−0.4210	0.0648	−0.4203	0.0759	−0.4195	0.0725	−0.4187	0.0882
	s^2 & $\hat{r}_D^2$	−0.4306	0.0027	−0.4311	0.0027	−0.4315	0.0027	−0.4324	0.0026
	s^*	−0.4028		−0.4025		−0.4022		−0.4018	
0.30	s^1 & $\hat{r}_D^1$	−0.3944	0.0562	−0.3932	0.0808	−0.3921	0.0833	−0.3911	0.0667
	s^2 & $\hat{r}_D^2$	−0.4018	0.0029	−0.4026	0.0028	−0.4033	0.0027	−0.4048	0.0026
	s^*	−0.3620		−0.3611		−0.3603		−0.3592	
0.20	s^1 & $\hat{r}_D^1$	−0.3601	0.0387	−0.3518	0.0990	−0.3501	0.0670	−0.3486	0.0637
	s^2 & $\hat{r}_D^2$	−0.3561	0.0011	−0.3566	0.0010	−0.3582	0.0027	−0.3615	0.0027
	s^*	−0.2867		−0.2871		−0.2848		−0.2812	
0.10	s^1 & $\hat{r}_D^1$	−0.2900	0.0116	−0.2857	0.0228	−0.2819	0.0371	−0.2781	0.0624
	s^2 & $\hat{r}_D^2$	−0.2630	0.0001	−0.2655	0.0004	−0.2687	0.0000	−0.2760	0.0000
	s^*	−0.2227		−0.2174		−0.2121			
0.05	s^1 & $\hat{r}_D^1$	−0.2259	0.0071	−0.2183	0.0076	−0.2126	0.0078	N.A.	
	s^2 & $\hat{r}_D^2$	−0.1629	0.0000	−0.1670	0.0000	−0.1765	0.0000		

Table 3. Singularity exponent s obtained from finite element analysis with $\psi = 0°$ and the corresponding analytical tensile results, as well as the range of dominance $\hat{r}_D$ of the tensile solution obtained from the radial variation of $\sigma_{\theta\theta}$ component of stress. Notations are the same as in Table 1. The material parameters are $E^{(1)}/E^{(2)} = 0.2, \rho^{(1)}/\rho^{(2)} = 1$.

α		β			
		0.001		0.15	
		s	$\hat{r}_D$	s	$\hat{r}_D$
	s^*	−0.3710		N.A.	
0.30	s^1 & $\hat{r}_D^1$	−0.3625	0.0070		
	s^*	−0.3291		−0.3073	
0.20	s^1 & $\hat{r}_D^1$	−0.3232	0.0067	−0.2931	0.0024
	s^*	−0.2236		−0.1927	
0.10	s^1 & $\hat{r}_D^1$	−0.2281	0.0058	−0.1752	0.0015
	s^*	−0.1536		N.A.	
0.05	s^1 & $\hat{r}_D^1$	−0.1557	0.0036		

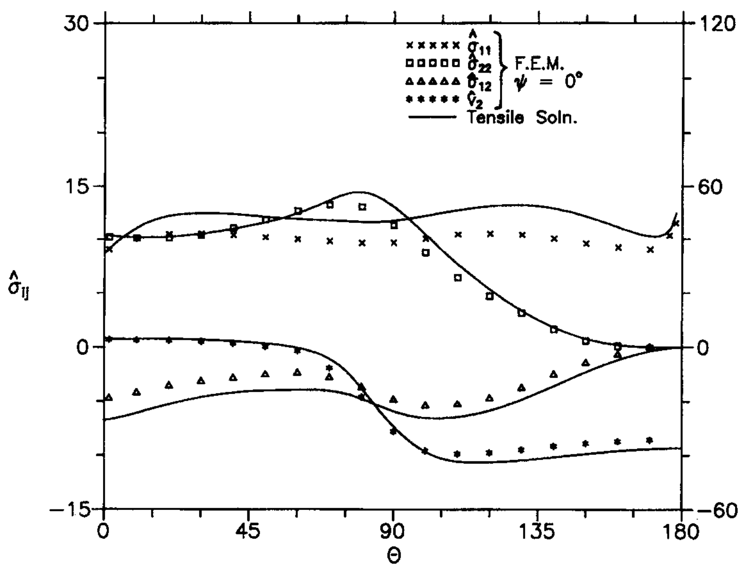

Figure 7. Comparison of angular variation of stress and velocity components at $\beta = 0.15$ obtained from finite element analysis at $\hat{r} = 10^{-4}$ for $\psi = 0°$ and the corresponding analytical tensile solution. The material parameters are $E^{(1)}/E^{(2)} = 0.2, \rho^{(1)}/\rho^{(2)} = 1, \alpha = 0.20$.

Next, the range of dominance $\hat{r}_D^1$ and $\hat{r}_D^2$ of the asymptotic solutions along $\theta = 0°$ and $45°$, respectively (based on $\hat{\sigma}_{\theta\theta}$ and $\hat{\sigma}_{r\theta}$ stress), are examined. It must be mentioned at the outset that attention is focused here only on the physically most relevant stress component, viz., $\sigma_{\theta\theta}$ for the tensile-type field and $\sigma_{r\theta}$ for the shear-type field. In interpreting the results for $\hat{r}_D$, it must be recalled that the maximum plastic zone extent is between 0.2 and $0.8(|\mathbf{K}|/\sigma_0^{(1)})^2$. From Tables 1 and 2 it can be seen that the range of dominance at $\theta = 45°$ is smaller than that directly ahead of the crack tip. In Table 1, $\hat{r}_D^1$ is found to decrease monotonically with a decrease in α at a fixed crack speed β and also with an increase in β at a fixed α. A comparative study of the Tables 1 and 2 shows that $\hat{r}_D^1$ for the shear field is larger than the tensile field at any given α and β. Further, on comparing Tables 1 and 3 it is found that the range of dominance of the tensile solution is less for the bi-material with a stiffer substrate.

In addition to the singularity strength, the finite element results for the near-tip angular variation of the stress and velocity components are compared with the analytical results in order to establish their validity. Attention is restricted only to the variation of the field variables in the ductile phase. Since the finite element results are computed at the integration stations which are arranged in a rectangular grid near the crack tip, a post-process smoothening procedure [19] was adopted for obtaining the angular variation of stresses and velocities on a semi-circular contour around the crack tip. The radius of the above near-tip semi-circular countour was chosen as $10^{-4}(|\mathbf{K}|/\sigma_0^{(1)})^2$ which is of the order of 1/10000 of the plastic zone size. In Figure 7, the angular variations of the normalized cartesian stress components $\hat{\sigma}_{ij}$ and th $\hat{v}_2$ velocity component obtained from the finite element results along the above-mentioned semi-circular countour are presented for the bi-material with $E^{(1)}/E^{(2)} = 0.2, \rho^{(1)}/\rho^{(2)} = 1, \alpha = 0.2$ corresponding to $\psi = 0°$ and crack speed $\beta = 0.15$. Also shown in this figure are the variations based on the analytical tensile solution [12]. In plotting the analytical solution, eqs. (1) and (2) are employed along with the value of the amplitude factor A which is determined

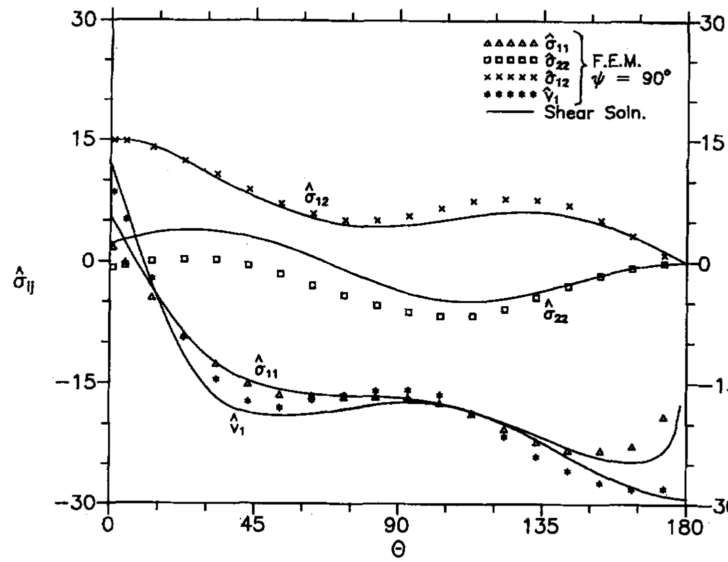

Figure 8. Comparison of angular variation of stress and velocity components at $\beta = 0.2$ obtained from finite element analysis at $\hat{r} = 10^{-4}$ for $\psi = 90°$ and the corresponding analytical shear solution. The material parameters are $E^{(1)}/E^{(2)} = 1, \rho^{(1)}/\rho^{(2)} = 1, \alpha = 0.25$.

as explained earlier in this section. A similar comparison between the analytical shear solution and the finite element results for the bi-material with $E^{(1)}/E^{(2)} = 1, \rho^{(1)}/\rho^{(2)} = 1, \alpha = 0.25$ is presented in Figure 8. The crack speed $\beta = 0.2$ and the value of ψ used to generate the finite element results is 90°. It can be seen from these figures that the finite element results for the all-around angular stress and velocity distributions agree well with the asymptotic fields. The above comparisons of the singularity orders and the near-tip angular stress and velocity distributions show that the asymptotic soluion [12] is valid near the crack tip.

3.4. Near-tip stress distribution and crack opening profiles

It is important to understand the influence of crack speed on the near-tip angular variation of stress components for various bi-materials. Also, the effect of changing the stiffness and density ratio of the bi-material on the angular stress variation at a fixed crack speed should be assessed. In Figures 9–11, the near-tip angular variation (at a radius $r = 10^{-4}(|\mathbf{K}|/\sigma_0^{(1)})^2$) of the normalized stress components obtained from finite element analysis corresponding to $\psi = 0°$ are shown for three different bi-material combinations with the same strain hardening level $\alpha = 0.25$. Results are displayed for crack speeds $\beta = 0.001$ and 0.25 in these figures.

Figure 9 shows the effect of crack speed for the bi-material with $E^{(1)}/E^{(2)} = 1, \rho^{(1)}/\rho^{(2)} = 1$. The most noticeable effect of crack speed is in decreasing $\hat{\sigma}_{11}$ and $\hat{\sigma}_{22}$ and, hence, the triaxial stress $\hat{\sigma}_{kk}/3$, in the region ahead of the crack tip. The reduction in the opening stress $\hat{\sigma}_{22}$ and the hydrostatic stress ahead of the crack tip with an increase in crack speed is mainly due to material inertia operating inside the crack tip plastic zone of the ductile phase. Further, it must be noted from Figure 9 that the upward turn in $\hat{\sigma}_{11}$ occurs closer to the crack flank ($\theta \to 180°$) at a higher crack speed. However, crack speed does not significantly affect the $\hat{\sigma}_{12}$ component of stress all around the crack tip.

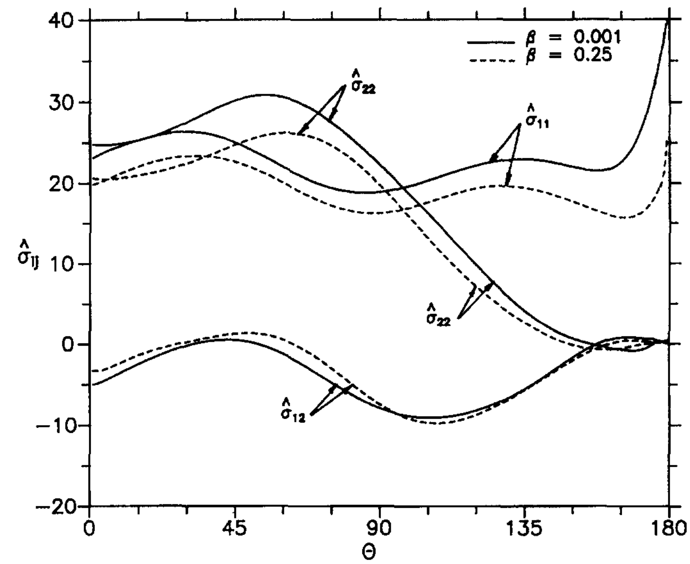

Figure 9. Effect of crack speed on the angular variation of stress components at $\hat{r} = 10^{-4}, \psi = 0°$ corresponding to the bi-material combination with $E^{(1)}/E^{(2)} = 1, \rho^{(1)}/\rho^{(2)} = 1, \alpha = 0.25$.

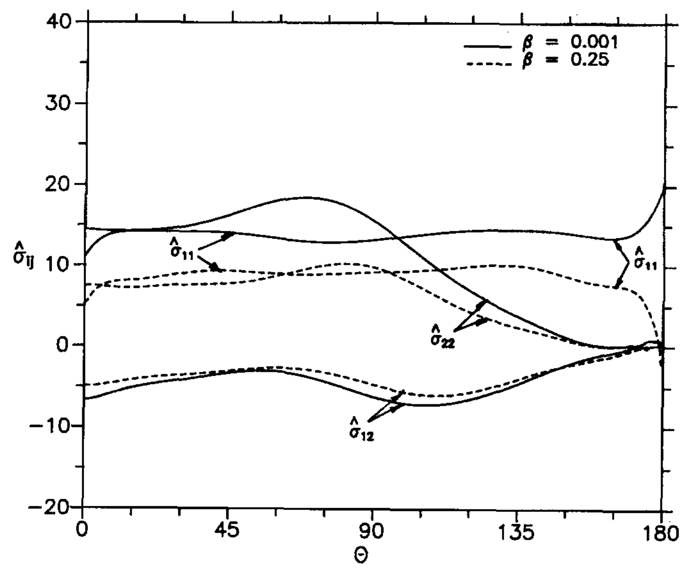

Figure 10. Effect of crack speed on the angular variation of stress components at $\hat{r} = 10^{-4}, \psi = 0°$ corresponding to the bi-material combination with $E^{(1)}/E^{(2)} = 0.2, \rho^{(1)}/\rho^{(2)} = 1, \alpha = 0.25$.

The influence of crack speed on the near-tip angular stress variation for the bi-material with $E^{(1)}/E^{(2)} = 0.2, \rho^{(1)}/\rho^{(2)} = 1$ is presented in Figure 10. This figure is plotted to the same scale as Figure 9 to facilitate direct comparison. It can be seen from Figure 10 that crack speed has a more significant effect on the near-tip stress variations for the bi-material with $E^{(1)}/E^{(2)} = 0.2$. Thus, while $\hat{\sigma}_{22}$ and $\hat{\sigma}_{11}$ ahead of the crack tip for $E^{(1)}/E^{(2)} = 0.2$ (Figure 10) exhibit a reduction of about 50 percent as β increases from 0.001 to 0.25, they decrease by only 20 percent for $E^{(1)}/E^{(2)} = 1$ (see Figure 9). Further, it is interesting to note

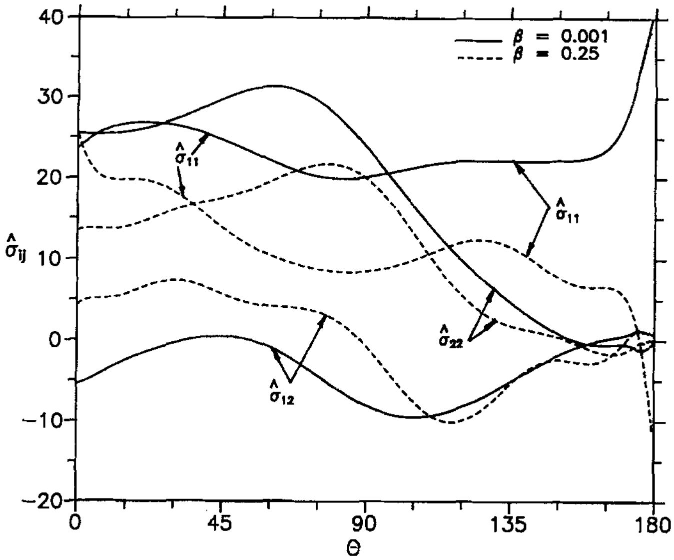

Figure 11. Effect of crack speed on the angular variation of stress components at $\hat{r} = 10^{-4}$, $\psi = 0°$ corresponding to the bi-material combination with $E^{(1)}/E^{(2)} = 1, \rho^{(1)}/\rho^{(2)} = 0.3, \alpha = 0.25$.

in Figure 10 that while the curve corresponding to $\hat{\sigma}_{11}$ at $\beta = 0.001$ shows an upward turn close to $\theta = 180°$, a sharp downward turn is exhibited by the curve pertaining to $\beta = 0.25$. This implies that while the state of stress at the crack flank is tensile at low crack speed, it becomes compressive at high crack speed.

Figure 11 corresponds to the case where $E^{(1)}/E^{(2)} = 1$ and $\rho^{(1)}/\rho^{(2)} = 0.3$. It is observed from this figure that when the two materials have different densities, there is a phenomenal effect of crack speed on the near-tip stress variation. The opening stress $\hat{\sigma}_{22}$ ahead of the crack tip in Figure 11 decrease by as much as 50 percent as crack speed β increases from 0.001 to 0.25. While $\hat{\sigma}_{11}$ close to $\theta = 0°$ is almost the same for the two crack speeds, it decreases everywhere else around the crack tip with elevation in crack speed. Further, $\hat{\sigma}_{11}$ becomes even more compressive at $\beta = 0.25$ than the case with $E^{(1)}/E^{(2)} = 0.2$ (see Figure 10), while a tensile stress state prevails at the crack flank at low β. It is also observed from Figure 11 that the angular distribution of $\hat{\sigma}_{12}$ changes significantly with an increase in crack speed β. Thus, it becomes positive ahead of the crack tip at high crack speed, whereas it is negative at low crack speed. This feature is quite unlike Figures 9 and 10, where $\hat{\sigma}_{12}$ is found to be almost unaffected by an increase in crack speed.

A direct comparison in Figures 9 and 10 reveals the effect of elastic stiffness mismatch on the near-tip stress variation at a fixed crack speed β since identical scales are used in these figures. The magnitude of $\hat{\sigma}_{11}$ and $\hat{\sigma}_{22}$ all around the crack tip (at fixed radius) decreases irrespective of the crack speed when the elastic substrate is stiffer. This is a consequence of the fact that the strength of the singularity $|s|$ is less when the substrate is stiffer for a given strain hardening parameter α and crack speed β (compare Tables 1 and 3). Further, the stress state near the crack flank becomes compressive at high crack speed for the case with stiffer substrate. As will be seen later in connection with Figure 13, the presence of a compressive stress parallel to the crack flank behind the crack tip at high crack speed for the bi-material with $E^{(1)}/E^{(2)} = 0.2$ inhibits the opening of the crack face. The effect of density mismatch can be

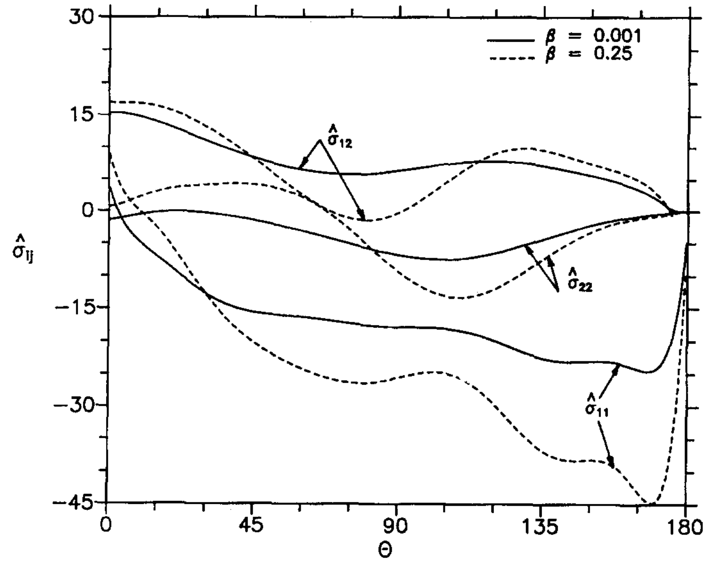

Figure 12. Effect of crack speed on the angular variation of stress components at $\widehat{r} = 10^{-4}$, $\psi = 90°$ corresponding to the bi-material combination with $E^{(1)}/E^{(2)} = 1, \rho^{(1)}/\rho^{(2)} = 0.3, \alpha = 0.4$.

appreciated from a comparative study of Figures 9 and 11. At low crack speed ($\beta = 0.001$), this mismatch has no effect on the stress distribution since the inertia term is insignificant. Its influence can be noticed by examining the curves in Figures 9 and 11 corresponding to a high crack speed $\beta = 0.25$. For the bi-material with $\rho^{(1)}/\rho^{(2)} = 0.3, \widehat{\sigma}_{11}$ and $\widehat{\sigma}_{22}$ are significantly less in magnitude at $\beta = 0.25$ as compared with the bi-material with $\rho^{(1)}/\rho^{(2)} = 1$.

Next, the effect of crack speed on the shear-type solution is examined. It is found that crack speed has negligible effect on the near-tip angular stress distribution of the shear-type solution for the bi-material with no mismatch in elastic stiffness and density. For example, the change in all-around stress components due to an increase in crack speed β from 0.001 and 0.25 for such a bi-material with $\alpha = 0.4$ corresponding to $\psi = 90°$ is restricted to less than 5 percent. Now, the effect of crack speed on the near-tip angular distribution of stress components for the bi-material with $E^{(1)}/E^{(2)} = 1, \rho^{(1)}/\rho^{(2)} = 0.3, \alpha = 0.4$ corresponding to $\psi = 90°$ is displayed in Figure 12. It can be noticed from this figure that the angular variations of stress components exhibit a significant change with an increase in crack speed. In particular, it can be observed that for θ greater than about 30°, there is a dramatic difference in the variation of the $\widehat{\sigma}_{11}$ stress component.

Finally, the effect of remote mode-mixity ψ, crack speed β and strain hardening α of the ductile phase on the near-tip crack profile in the ductile material is investigated. The extent of crack opening at a finite distance the tip is found to reduce as ψ increases from 0°. However, the crack profiles for ψ in the range from 0° to 30° are almost the same very close to the crack tip ($\widehat{x}_1 < 0.002$), irrespective of crack speed. This is consistent with the fact that a tensile-type field is definitely attained near the tip for this range of ψ. The normalized crack opening profiles $\widehat{u}_2 = u_2/(|\mathbf{K}|^2/E^{(1)}\sigma_0^{(1)})$ in the ductile phase with normalized distance $\widehat{x}_1$ behind the crack tip are shown in Figure 13 corresponding to $\psi = 0°$. Results are presented in this figure for two crack speeds ($\beta = 0.001$ and 0.25) corresponding to $E^{(1)}/E^{(2)} = 1$ and 0.2 (with $\rho^{(1)}/\rho^{(2)} = 1$) and $\alpha = 0.1$. From this figure, it can be readily seen that irrespective

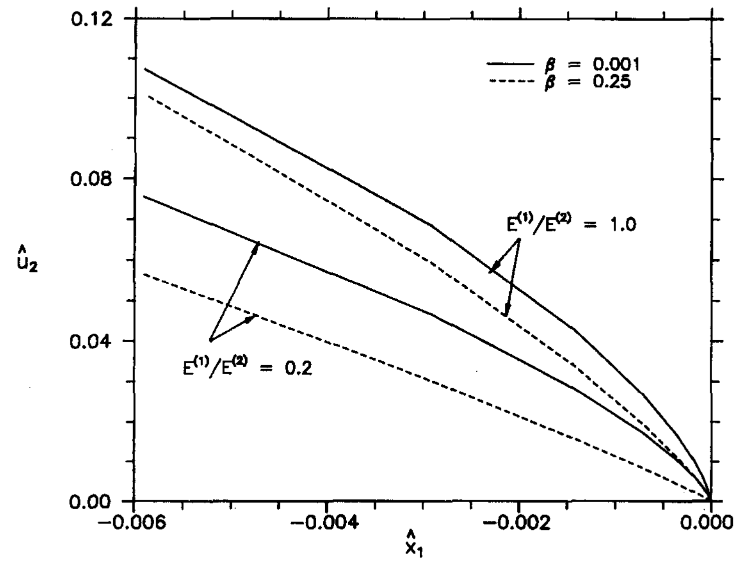

Figure 13. Normalized crack opening profiles corresponding to two crack speeds at $\psi = 0°$ for two bi-material combinations with $\rho^{(1)}/\rho^{(2)} = 1, \alpha = 0.10$.

of crack speed, the extent of crack opening in the ductile phase is less when the substrate is stiffer. Further, the reduction in crack profile with an increase in β in Figure 13 shows that the ductile phase becomes more resistant to opening at high crack speed due to material inertia. The above effect is more pronounced for the bi-material with the stiffer substrate. This is due to the presence of a compressive stress parallel to the crack flank behind the crack tip at high crack speed for the bi-material with the stiffer substrate as noted in connection with Figure 10. Also, it is found that the decrease in crack opening profile with an increase in crack speed is more transparent at low strain hardening α. This implies that the length scale over which inertia affects the near-tip crack opening profile is restricted to a smaller region near the crack tip for the case of a flexible substrate or that pertaining to high strain hardening of the ductile phase.

3.5. THEORETICAL DYNAMIC FRACTURE TOUGHNESS

In this section, theoretical predictions are made for the variation of the dynamic fracture toughness with crack velocity for interface crack growth under a predominantly tensile (opening) mode. Thus, attention is restricted only to the case of remote $\psi = 0°$, which gives rise to near-tip mixity m close to unity. Here, $|\mathbf{K}|$ is used as a measure of the interface dynamic fracture toughness under small-scale yielding conditions. The main objective is to assess the influence of strain hardening of the ductile phase and stiffness mismatch of the two phases on the $|\mathbf{K}_d|$ versus crack speed relation. For this purpose, a ductile fracture criterion based on the attainment of a critical opening displacement of the crack flank in the ductile phase is employed. The above criterion requires that a critical opening displacement $u_2 = (u_2)_c$ of the upper crack flank (corresponding to the ductile phase) should be maintained at a small micro-structural distance $r = (r)_c$ behind the crack tip for continued crack growth. The motivation for employing this criterion stems from experimental observations of self-similar crack profiles during crack growth in homogeneous ductile solids. On employing the above

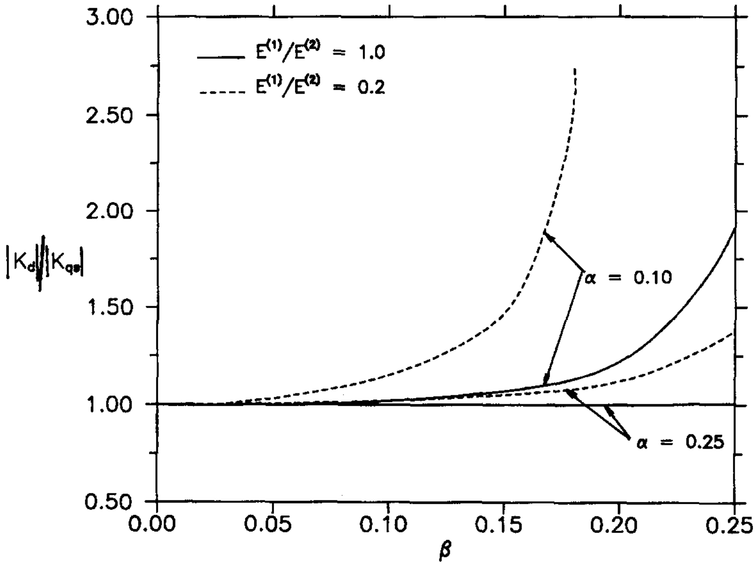

Figure 14. Variation of $|\mathbf{K}_d|/|\mathbf{K}_{qs}|$ with crack speed at $\psi = 0°$ for different bi-material combinations with $\rho^{(1)}/\rho^{(2)} = 1$ corresponding to a fixed value of micro-structural parameter $u_c/(\epsilon_0^{(1)} r_c) = 35.0$.

criterion for both quasi-static crack growth and crack propagation at a higher speed, the ratio of the dynamic fracture toughness $|\mathbf{K}_d|$ to the quasi-static limit $|\mathbf{K}_{qs}|$ can be obtained (see [8] for details).

The variation of the theoretically predicted $|\mathbf{K}_d|/|\mathbf{K}_{qs}|$ with crack speed β is shown in Figure 14. In this work, the critical value of $u_2/(\epsilon_0^{(1)} r)$ is taken as 35 (see also [8]). Results are presented for two stiffness ratios, $E^{(1)}/E^{(2)} = 1.0$ and 0.2, (but with no density mismatch) and two values of strain hardening, $\alpha = 0.25$ and 0.10. As already mentioned, these results pertain to $\psi = 0°$. On examining the curves depicted in the figure, it can be inferred that the elevation of the dynamic fracture toughness over the quasi-static value is higher for a bi-material with a stiffer substrate, particularly at high crack speeds. Further, it should be noted that at high crack speeds, the above elevation in the dynamic fracture toughness is considerably enhanced when the ductile phase exhibits lower strain hardening. The above results indicate that the effect of material inertia (operating inside the crack-tip plastic zone of the ductile phase) in enhancing the resistance to dynamic crack propagation along the interface is more pronounced when the elastic substrate is stiffer and when the ductile phase exhibits low strain hardening. The above conclusion is also corroborated by the observations made on the near-tip stress fields in Section 3.4.

4. Conclusions

In this paper, steady dynamic crack growth along a ductile-brittle interface under plane strain, small-scale yielding conditions has been analysed using a finite element procedure. The important conclusions of this work are as follows:

(1) For the bi-material with $E^{(1)}/E^{(2)} = 1, \rho^{(1)}/\rho^{(2)} = 1$, the mode-mixity m near the tip approaches the value predicted by the analytical tensile solution [12] when $0° \leqslant \psi \leqslant 30°$, and tends towards that predicted by the shear solution [12] when $\psi = 90°$. The transition

from a tensile-type to a shear-type field occurs between $\psi = 60°$ and $90°$. For the bi-material with a stiffer substrate, m approaches the near-tip limit set by the analytical tensile solution when $0° \leqslant \psi \leqslant 90°$. Shear-type solutions are obtained when the remote normal stress on the interface line is compressive (i.e., $\psi > 90°$).

(2) Crack speed reduces the singularity strength $|s|$ associated with the tensile-type solution, particularly at low values of α. But, crack speed has negligible effect on s for the shear solution. For the bi-material with the stiffer substrate $|s|$ is lower for a fixed α and β. In general, the values of s as well as the all-around angular stress and velocity distributions obtained from the finite element analyses match quite well with the analytical results [12]. Thus, the validity of the analytical solutions of [12] near the tip is established.

(3) The range of dominance of the tensile solution is found to decrease with a decrease in α at a fixed crack speed β, and also with an increase in β at a fixed α. Further, the range of dominance at $\theta = 45°$ is smaller than that directly ahead of the crack tip. Introduction of a stiffer substrate reduces the range of dominance of the tensile field. The shear field exhibits a larger range of dominance than the tensile field at a given α and β.

(4) The most noticeable effect of crack speed on the near-tip angular stress distribution for the tensile-type field is in decreasing the opening stress $\widehat{\sigma}_{22}$ and the triaxial stress ahead of the tip. The above effects are more pronounced when the substrate is stiffer or if there is a density mismatch. Introduction of a stiffer substrate reduces the stresses all around the crack tip, irrespective of crack speed.

(5) The decrease in the near-tip crack opening profile in the ductile phase with an increase in crack speed corresponding to the tensile-type solution is more significant for the bi-material with a stiffer substrate. This can result in higher elevation in the dynamic fracture toughness over the quasi-static limit for such a bi-material when crack propagation occurs in a predominantly opening mode, especially at high crack speeds. Also, this effect is expected to be more pronounced when the ductile phase has low strain hardening.

References

1. H.V. Tippur and A.J. Rosakis, Quasi-static and dynamic crack growth along bimaterial interfaces: a note on crack-tip field measurements using coherent gradient sensing. *Experimental Mechanics* 31 (1991) 243–251.
2. P.P Casteñeda and P.A. Mataga, Stable crack growth along a brittle/ductile interface – I. Near-tip fields. *International Journal of Solids and Structures* 27 (1991) 105–133.
3. W.J. Drugan, Near-tip fields for quasi-static crack growth along a ductile-brittle interface. *ASME Journal of Applied Mechanics* 58 (1991) 111–119.
4. J.T. Leighton, C.R. Champion and L.B. Freund, Asymptotic analysis of steady dynamic crack growth in an elastic-plastic material. *Journal of Mechanics and Physics of Solids* 35 (1987) 541–563.
5. J.D. Achenbach, M.F. Kanninen and C.H. Popelar, Crack-tip fields for fast fracture of an elastic-plastic material. *Journal of Mechanics and Physics of Solids* 29 (1981) 211–225.
6. S. Östlund and P. Gudmundson, Asymptotic fields for dynamic fracture of linear hardening solids. *International Journal of Solids and Structures* 24 (1988) 1141–1158.
7. P.S. Lam and L.B. Freund, Analysis of dynamic growth of a tensile crack in an elastic-plastic material. *Journal of Mechanics and Physics of Solids* 33 (1985) 153–167.
8. R. Narasimhan and C.S. Venkatesha, A finite element analysis of plane strain dynamic crack growth in materials displaying the Bauschinger effect. *International Journal of Fracture* 61 (1993) 139–157.
9. W. Yang, Z. Suo and C.F. Shih, Mechanics of dynamic debonding. *Proceedings of the Royal Society of London – A* 433 (1991) 679–697.
10. X. Deng, Dynamic crack growth along elastic-plastic interfaces. *International Journal of Solids and Structures* 30 (1993) 2937–2951.
11. K. Ranjith and R. Narasimhan, Asymptotic and finite element analyses of mode III dynamic crack growth at a ductile-brittle interface. *International Journal of Fracture* 76 (1996) 61–77.

12. K. Ranjith and R. Narasimhan, Asymptotic fields for dynamic crack growth at a ductile-brittle interface. To appear in *Journal of Mechanics and Physics of Solids* (1996).
13. C.Y. Lo, T. Nakamura and A. Kushner, Computational analysis of dynamic crack propagation along a bi-material interface. *International Journal of Solids and Structures* 31 (1994) 145–168.
14. R. Narasimhan and A.J. Rosakis, A finite element analysis of small scale yielding near a stationary crack under plane stress. *Journal of Mechanics and Physics of Solids* 36 (1988) 77–117.
15. L.B. Freund and A.S. Douglas, The influence of inertia on elastic-plastic antiplane shear crack growth. *Journal of Mechanics and Physics of Solids* 30 (1982) 59–74.
16. T.J.R. Hughes, Generalization of selective/reduced integration procedures to anisotropic and non-linear media. *International Journal for Numerical Methods in Engineering* 15 (1980) 1413–1418.
17. C.F. Shih and R.J. Asaro, Elastic-plastic analysis of cracks on bi-material interfaces. Part I: Small scale yielding. *ASME Journal of Applied Mechanics* 55 (1988) 299–316.
18. K. Bose and P.P. Castañeda, Stable crack growth under mixed-mode conditions. *Journal of Mechanics and Physics of Solids* 40 (1992) 1053–1103.
19. P.S. Lam and R.M. McMeeking, Analysis of steady quasistatic crack growth in plane strain tension in elastic-plastic materials with non-isotropic hardening. *Journal of Mechanics and Physics of Solids* 32 (1984) 395–414.